

The properties of supermassive stars in galaxy merger driven direct collapse I: models without rotation

L. Haemmerlé

Département d'Astronomie, Université de Genève, chemin Pegasi 51, CH-1290 Versoix, Switzerland

Preprint online version: March 5, 2025

ABSTRACT

Context. The formation of the most massive quasars observed at high redshifts requires extreme accretion rates ($> 1 M_{\odot} \text{ yr}^{-1}$). Inflows of $10 - 1000 M_{\odot} \text{ yr}^{-1}$ are found in hydrodynamical simulations of galaxy mergers, leading to the formation of supermassive discs (SMDs) with high metallicities ($> Z_{\odot}$). Supermassive stars (SMSs) born in these SMDs could be the progenitors of the most extreme quasars.

Aims. Here, we study the properties of non-rotating SMSs forming in high metallicity SMDs.

Methods. Using the stellar evolution code `GENEC`, we compute numerically the hydrostatic structures of non-rotating SMSs with metallicities $Z = 1 - 10 Z_{\odot}$ by following their evolution under constant accretion at rates $10 - 1000 M_{\odot} \text{ yr}^{-1}$. We determine the final mass of the SMSs, set by the general-relativistic (GR) instability, by applying the relativistic equation of adiabatic pulsations to the hydrostatic structures.

Results. We find that non-rotating SMSs with metallicities $Z = 1 - 10 Z_{\odot}$ accreting at rates $10 - 1000 M_{\odot} \text{ yr}^{-1}$ evolve as red supergiant protostars until their final collapse. All the models reach the GR instability during H-burning. The final mass is $\sim 10^6 M_{\odot}$, nearly independently of the metallicity and the accretion rate.

Key words. stars: massive – stars: black holes

1. Introduction

In the last decade, a number of quasars, hosting supermassive black holes (SMBHs) with masses $10^6 - 10^9 M_{\odot}$, have been discovered at redshifts $z \geq 7$ (Wu et al. 2015; Bañados et al. 2018; Wang et al. 2018; Yang et al. 2020; Wang et al. 2021; Larson et al. 2023; Kokorev et al. 2023; Kovács et al. 2024; Bogdán et al. 2024; Maiolino et al. 2024). The young age of the universe at these redshifts implies an extremely rapid formation process for these SMBHs (Woods et al. 2019; Haemmerlé et al. 2020). A promising scenario is direct collapse, that is the direct formation of a SMBH seed with mass $\geq 10^5 - 10^6 M_{\odot}$. In this scenario, the progenitor of the SMBH seed is a supermassive star (SMS) growing by accretion (Hosokawa et al. 2012, 2013; Umeda et al. 2016; Woods et al. 2017, 2021, 2024; Haemmerlé et al. 2018b,a, 2019; Herrington et al. 2023; Nandal et al. 2023, 2024) until it reaches the general-relativistic (GR) instability (Chandrasekhar 1964; Haemmerlé 2020, 2021a,b, 2024; Saio et al. 2024; Nagele & Umeda 2024).

Direct collapse requires special conditions. In the collapse of an isolated primordial halo, molecular cooling by H_2 is found to limit the stellar mass to $\sim 100 M_{\odot}$ (e.g. Bromm et al. 2002; Klessen & Glover 2023). Only in the presence of a strong Lyman-Werner flux, that dissociates H_2 , a zero-metallicity SMS can form, under accretion at rates $0.01 - 1 M_{\odot} \text{ yr}^{-1}$, in the collapse of the atomically cooled halo (e.g. Haiman et al. 1997; Omukai 2001; Dijkstra et al. 2008; Bromm & Loeb 2003; Latif et al. 2013; Regan et al. 2017; Chon et al. 2018). At a redshift $z \sim 7$, the age of the universe is a fraction of a Gyr, so that accretion rates $> 1 M_{\odot} \text{ yr}^{-1}$ are required to form objects like ULAS J1120+0641 (Mortlock et al. 2011), ULAS J1342+0928 (Bañados et al. 2018), DELS J0038-1527 (Wang et al. 2018), UHS J1007+2115 (Yang et al. 2020) or J0313-1806 (Wang et al.

2021), hosting SMBHs with masses $\sim 10^9 M_{\odot}$. We see that the rates of atomically cooled halos are just at the limit of what is required to form the most massive quasars observed at high redshifts.

A more efficient route of direct collapse is the case of the merger of massive gas-rich galaxies (Mayer et al. 2010, 2015, 2024; Zwick et al. 2023). In this scenario, inflows of $10 - 1000 M_{\odot} \text{ yr}^{-1}$ are triggered down to parsec scales (see Figure 5 of Mayer et al. 2024), which results in the formation of a rotationally supported supermassive disc (SMD) with mass $\sim 10^9 M_{\odot}$. Cosmological simulations indicate that such SMDs are metal-rich, with a metallicity in the range $1 - 10 Z_{\odot}$, typically $3 Z_{\odot}$ (see Figure 7 of Mayer et al. 2024).

Here, we study for the first time the properties of SMSs forming by accretion in the conditions of galaxy merger driven direct collapse, that is with metallicities $> Z_{\odot}$ and accretion rates $10 - 1000 M_{\odot} \text{ yr}^{-1}$. We derive numerically the properties of such SMSs during their hydrostatic accretion phase as well as their final masses at collapse, set by the GR instability, which provides an estimate of the mass of the SMBH seeds formed in this scenario. This work is the first of a series, and here we consider only the non-rotating case. The method is described in Sect. 2, the results are presented in Sect. 3 and discussed in Sect. 4, and we conclude in Sect. 5.

2. Method

2.1. Hydrostatic structures

The hydrostatic structures are computed with `GENEC` (Eggenberger et al. 2008), a one-dimensional hydrostatic stellar evolution code that solves numerically the equations of stellar structure with the Henyey method. The code includes

the GR Tolman-Oppenheimer-Volkoff corrections to hydrostatic equilibrium in the post-Newtonian approximation (Haemmerlé et al. 2018b). Accretion is included under the assumption of cold accretion (Haemmerlé et al. 2016). We start from an initial model of $M = 100 M_\odot$, and consider constant accretion at rates $\dot{M} = 10 - 100 - 1000 M_\odot \text{yr}^{-1}$. We use such a high initial mass because the rates considered are not consistent with gravity for lower masses (Haemmerlé et al. 2021).

The chemical composition of the initial model and that of the accreted material are identical and are scaled with the solar abundances of Asplund et al. (2005). For each metallicity $Z = 1 - 3 - 10 Z_\odot$, the mass fraction of hydrogen (X) and of helium (Y) are set by extrapolation from the primordial and solar compositions:

$$Y = Y_0 + (Y_\odot - Y_0) \frac{Z}{Z_\odot} \quad (1)$$

$$X = 1 - Y - Z \quad (2)$$

where $Y_0 = 0.2484$ is the primordial helium mass fraction.

2.2. GR instability

We determine the GR instability point with the method of Chandrasekhar (1964). This method relies on a linear pulsation analysis of Einstein's field equations in spherical symmetry, assuming adiabatic perturbations to equilibrium. The pulsation equation reads

$$\begin{aligned} \frac{\omega^2}{c^2} \cdot r^2 e^{-a} \xi(r) = & \frac{r^2 e^{-a-3b}}{P + \rho c^2} \cdot \left(- \left(\Gamma_1 P \frac{e^{3a+b}}{r^2} (r^2 e^{-a} \xi(r))' \right)' \right) \\ & + \frac{e^{3a+b}}{r^2} \left(\frac{4}{r} P' - \frac{P'^2}{P + \rho c^2} \right. \\ & \left. + \frac{8\pi G}{c^4} P (P + \rho c^2) e^{2b} \right) \cdot r^2 e^{-a} \xi(r) \end{aligned} \quad (3)$$

where $'$ denotes a derivative with respect to the radial coordinate r , ω is the pulsation frequency, ξ the radial displacement of the perturbation, Γ_1 the first adiabatic exponent, P the thermal pressure, ρ the relativistic mass density, c the speed of light, G the gravitational constant, and a and b are the coefficients of the metric:

$$ds^2 = -e^{2a}(cdt)^2 + e^{2b}dr^2 + r^2 d\theta^2 + r^2 \sin^2 \theta d\varphi^2 \quad (4)$$

Except ω and ξ , all the quantities involved in equation (3) refer to equilibrium.

Equation (3) is an eigenvalue problem

$$\frac{\omega^2}{c^2} f = \mathcal{L}f \quad (5)$$

for the Sturm-Liouville operator

$$\begin{aligned} \mathcal{L}f(r) = & \frac{r^2 e^{-a-3b}}{P + \rho c^2} \cdot \left(- \left(\Gamma_1 P \frac{e^{3a+b}}{r^2} f'(r) \right)' \right) \\ & + \frac{e^{3a+b}}{r^2} \left(\frac{4}{r} P' - \frac{P'^2}{P + \rho c^2} + \frac{8\pi G}{c^4} P (P + \rho c^2) e^{2b} \right) \cdot f(r) \end{aligned} \quad (6)$$

with $f(r) = r^2 e^{-a} \xi(r)$ and the boundary conditions $\xi(0) = 0$ and $\delta P(R) = 0$. The operator \mathcal{L} is self-adjoint for the scalar product

$$\langle f|g \rangle := \int_0^R \frac{P + \rho c^2}{r^2} e^{a+3b} f(r)g(r)dr \quad (7)$$

As a consequence, the spectral theorem implies that there exists an orthonormal basis (of the real vector space of functions satisfying the required boundary conditions) whose elements are the eigenvectors of \mathcal{L} . In other words, any function $f(r)$ that satisfies the required boundary conditions can be written as a linear combination of eigenfunctions f_i with eigenvalue λ_i :

$$f = \sum_i c_i f_i \quad (8)$$

And the different f_i are all orthonormal to each other. It implies that

$$\langle f|\mathcal{L}f \rangle = \sum_{i,j} c_i c_j \langle f_i|\mathcal{L}f_j \rangle = \sum_{i,j} c_i c_j \lambda_j \underbrace{\langle f_i|f_j \rangle}_{=\delta_{ij}} = \sum_i c_i^2 \lambda_i \quad (9)$$

We see that, if there is any function $f(r)$ whose scalar product with its image through \mathcal{L} is negative, then there exists necessarily at least one negative eigenvalue $\lambda_i < 0$. Indeed, if the left-hand side of Equation (9) is negative, the right-hand side must also be negative, which is possible only if one of the λ_i is negative. And if an eigenvalue of \mathcal{L} is negative, it implies that there are solutions to Equation (3) with an imaginary pulsation frequency, that is the star is GR unstable.

By applying the scalar product $\langle f|\cdot \rangle$ with $f(r) = r^2 e^{-a} \xi(r)$ on the two sides of Equation (3), we obtain

$$\begin{aligned} \omega^2 \int_0^R e^{-a+3b} \left(1 + \frac{P}{\rho c^2} \right) \rho r^2 \xi^2(r) dr & \\ = - \int_0^R r^2 e^{-a} \xi(r) \left(\Gamma_1 P \frac{e^{3a+b}}{r^2} (r^2 e^{-a} \xi(r))' \right)' dr & \\ + 4 \int_0^R P' r e^{a+b} \xi^2(r) dr - \int_0^R \frac{P'^2 r^2 e^{a+b}}{P + \rho c^2} \xi^2(r) dr & \\ + \frac{8\pi G}{c^4} \int_0^R (P + \rho c^2) P r^2 e^{a+3b} \xi^2(r) dr & \end{aligned} \quad (10)$$

We can transform the first term on the right-hand side by an integration by parts (the boundary terms vanish):

$$\begin{aligned} \omega^2 \int_0^R e^{-a+3b} \left(1 + \frac{P}{\rho c^2} \right) \rho r^2 \xi^2(r) dr & \\ = \int_0^R \Gamma_1 P \frac{e^{3a+b}}{r^2} (r^2 e^{-a} \xi(r))'^2 dr & \\ + 4 \int_0^R P' r e^{a+b} \xi^2(r) dr - \int_0^R \frac{P'^2 r^2 e^{a+b}}{P + \rho c^2} \xi^2(r) dr & \\ + \frac{8\pi G}{c^4} \int_0^R (P + \rho c^2) P r^2 e^{a+3b} \xi^2(r) dr & \end{aligned} \quad (11)$$

This is Equation (61) of Chandrasekhar (1964). It corresponds to

$$\frac{\omega^2}{c^2} \langle f|f \rangle = \langle f|\mathcal{L}f \rangle \quad (12)$$

And as we saw in Equation (9), 'it is clear that a sufficient condition for the dynamical instability of a mass is that the right-hand side of [Equation (11)] vanishes for some chosen "trial function" ξ which satisfies the required boundary conditions' (Chandrasekhar 1964). The function $\xi(r)$ does not need to represent the actual perturbation to equilibrium, this is just an arbitrary trial function that allows to prove the existence of a negative

eigenvalue. For $\xi(r) = re^{a(r)}$, Equation (11) gives Equation (1) of Haemmerlé (2021a):

$$\frac{\omega^2}{c^2} I_0 = \sum_{i=1}^4 I_i \quad (13)$$

with

$$I_0 = \int_0^R e^{a+3b} (P + \rho c^2) r^4 dr \quad (14)$$

$$I_1 = 9 \int_0^R \Gamma_1 e^{3a+b} P r^2 dr \quad (15)$$

$$I_2 = 4 \int_0^R e^{3a+b} P' r^3 dr \quad (16)$$

$$I_3 = \frac{8\pi G}{c^4} \int_0^R e^{3(a+b)} P (P + \rho c^2) r^4 dr \quad (17)$$

$$I_4 = - \int_0^R e^{3a+b} \frac{P'^2}{P + \rho c^2} r^4 dr \quad (18)$$

The sufficient condition for instability obtained in this way is more efficient than GR hydrodynamical stellar evolution codes in capturing the GR instability (Haemmerlé 2021a; Nagele et al. 2022). Moreover, the trial function used approximates accurately the actual dynamical perturbation, which implies that this condition is close to an exact condition (Saio et al. 2024).

In the post-Newtonian limit, Equation (13) reduces to (Haemmerlé 2021b)

$$\omega^2 I = \int \beta P dV - \int \left(\frac{2GM_r}{rc^2} + \frac{8}{3} \frac{P}{\rho c^2} \right) \frac{GM_r}{r} dM_r \quad (19)$$

where β is the ratio of gas pressure to total pressure, $dV = 4\pi r^2 dr$, M_r is the Lagrangian coordinate and I is the moment of inertia.

3. Results

The evolutionary tracks on the Hertzsprung-Russell (HR) diagram of the models at $Z = 3 Z_\odot$ are shown in Figure 1. The luminosity L grows continuously with the stellar mass M , following nearly the Eddington limit:

$$L \simeq \frac{4\pi c G M}{\kappa} \quad (20)$$

where $\kappa \simeq 0.2(1 + X) \text{ cm}^2 \text{ g}^{-1}$ is the opacity, dominated by electron scattering. The effective temperature shows strong oscillations due to the low resolution in the outer layers, but the star remains a 'red supergiant protostar' (Hosokawa et al. 2012, 2013; Haemmerlé et al. 2018b) all along the evolution, following the Hayashi limit up to luminosities $10^{10} - 10^{11} L_\odot$.

The internal structure of some of the models are shown in Figures 2-3-4-5. Once the star is supermassive ($M \gtrsim 10^4 - 10^5 M_\odot$), it is made of a convective core, where convection is driven by H-burning, a 'radiative' zone (full of small transient convective zones), and a convective envelope due to the low temperatures and high opacities on the Hayashi limit. The convective envelope is thinner for larger accretion rates. Although the photospheric radius keeps growing, all the Lagrangian layers are contracting, except in the convective core, where the heat liberated by H-burning causes the gas to expand. We see again the oscillations of the surface already visible in Figure 1. Each expansion of the photospheric radius results in the deepening of

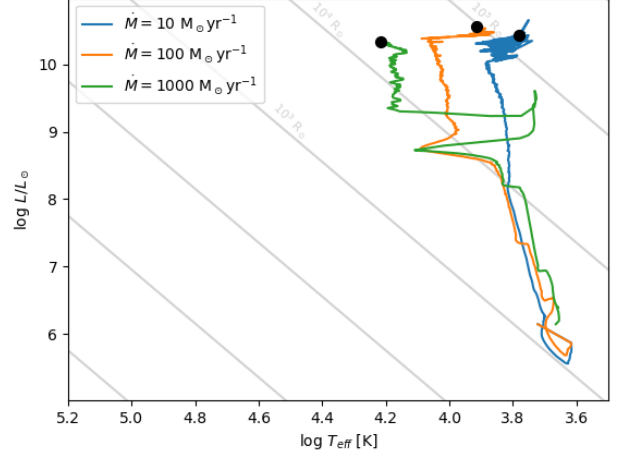


Fig. 1. HR diagram of the models at $Z = 3 Z_\odot$. The black circles indicate the point of GR instability.

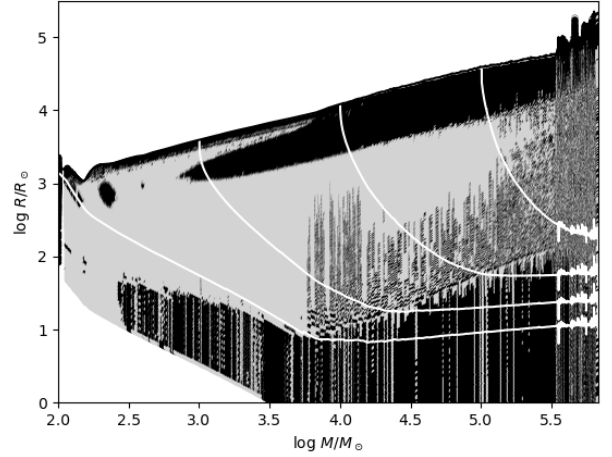


Fig. 2. Internal structure of the model at $Z = 3 Z_\odot$ and $\dot{M} = 10 M_\odot \text{ yr}^{-1}$, as a function of the stellar mass M . The convective zones are shown in black and the radiative zones in grey. The white curves are iso-masses (Lagrangian layers).

the convective envelope. Once it enters the radiative region, the gas accreted during such events keeps a memory of it, showing a higher density of transient convective zones compared to the other layers (see for instance the layers $10^4 M_\odot < M_r < 10^5 M_\odot$ in Figure 4). Inversely, the layers accreted during a contraction show a lower density of transient convective zones (see for instance the layers $10^4 M_\odot < M_r < 10^5 M_\odot$ in Figure 3).

The entropy profiles of the models at $Z = 3 Z_\odot$ are shown in Figures 6-7-8. On each profile, we can distinguish the convective core which is nearly isentropic, the radiative zone where entropy grows outwards, and the thin convective envelope where entropy decreases outwards, because of the non-adiabaticity of convection in the low density outer layers. We can see that, in the convective core, the entropy is growing due to the heat liberated by H-burning. In the radiative zone, for accretion rates $\dot{M} > 10 M_\odot \text{ yr}^{-1}$, the successive profiles superimpose to each

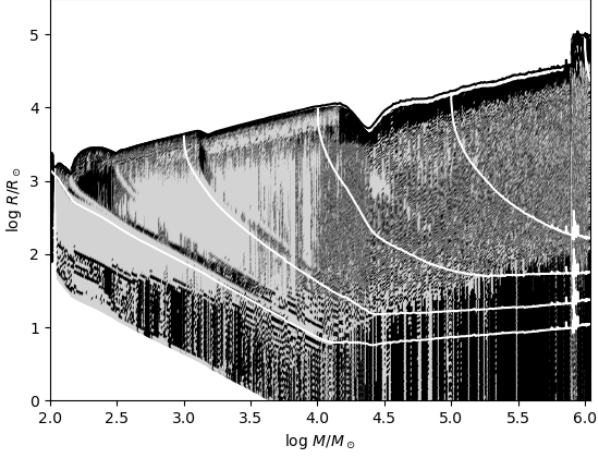


Fig. 3. Same as Figure 2 for the model at $Z = 3 Z_{\odot}$ and $\dot{M} = 100 M_{\odot} \text{ yr}^{-1}$.

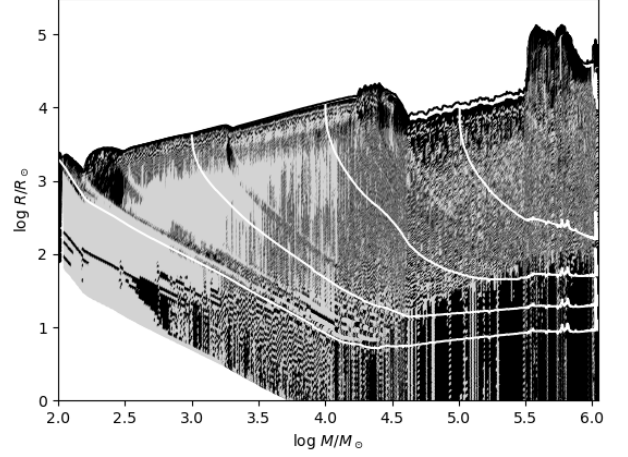


Fig. 5. Same as Figure 2 for the model at $Z = Z_{\odot}$ and $\dot{M} = 100 M_{\odot} \text{ yr}^{-1}$.

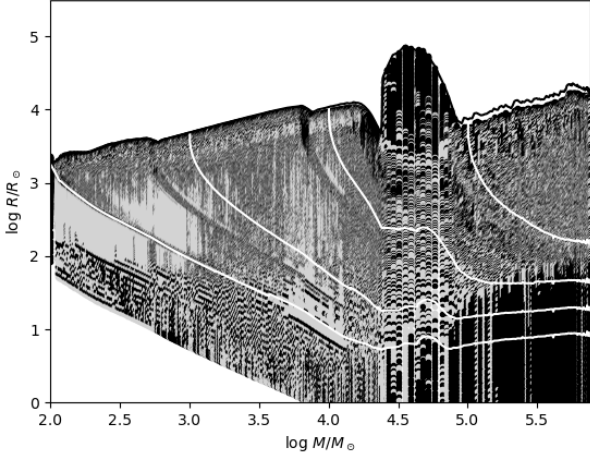


Fig. 4. Same as Figure 2 for the model at $Z = 3 Z_{\odot}$ and $\dot{M} = 1000 M_{\odot} \text{ yr}^{-1}$.

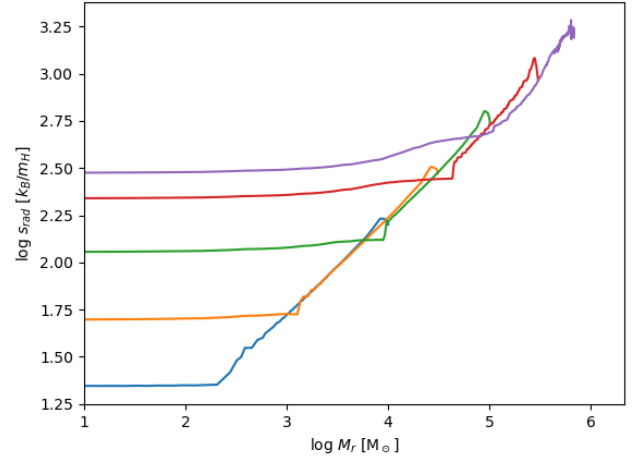


Fig. 6. Entropy profiles of the model at $Z = 3 Z_{\odot}$ and $\dot{M} = 10 M_{\odot} \text{ yr}^{-1}$ as a function of the Lagrangian coordinate, at different masses.

other, which shows that the evolution is adiabatic in this region of the star: the entropy losses are negligible in the short evolutionary timescale for such rapid accretion. In this case, the entropy profiles adjust on hylotropic profiles $s \propto M_r^{1/2}$ (Begelman 2010; Haemmerlé et al. 2019; Haemmerlé 2020). Departures from the hylotropic profiles are visible, which reflects the oscillations of the surface described above: due to the absence of entropy losses, each Lagrangian layer keeps memory of the accretion event. In particular, for the biggest expansion visible in Figure 4, at a mass $\sim 30\,000 M_{\odot}$, we find a plateau in the entropy profiles of Figure 8 around the Lagrangian layers $M_r \sim 30\,000 M_{\odot}$. Only for accretion rates $\dot{M} \leq 10 M_{\odot} \text{ yr}^{-1}$ the evolutionary timescale is long enough for the losses of entropy due to radiative transfer to be visible in the radiative zone.

The final masses at GR instability, obtained with Equation (19), are shown for all the models in Table 1 and Figure 9. All the final masses range in the interval $0.6 - 1.2 \times 10^6 M_{\odot}$, with a very weak dependence on the

Table 1. Stellar mass (in $10^6 M_{\odot}$) at the onset of GR instability for the indicated metallicities and accretion rates.

| | $10 M_{\odot} \text{ yr}^{-1}$ | $100 M_{\odot} \text{ yr}^{-1}$ | $1000 M_{\odot} \text{ yr}^{-1}$ |
|--------------------|--------------------------------|---------------------------------|----------------------------------|
| $Z = Z_{\odot}$ | 0.763 | 1.11 | 0.759 |
| $Z = 3 Z_{\odot}$ | 0.678 | 1.10 | 0.760 |
| $Z = 10 Z_{\odot}$ | | | 0.663 |

metallicity. For accretion rates $\dot{M} \lesssim 100 M_{\odot} \text{ yr}^{-1}$, the final mass increases as the accretion rate increases. But for $\dot{M} \gtrsim 100 M_{\odot} \text{ yr}^{-1}$ the final mass is a decreasing function of the accretion rate.

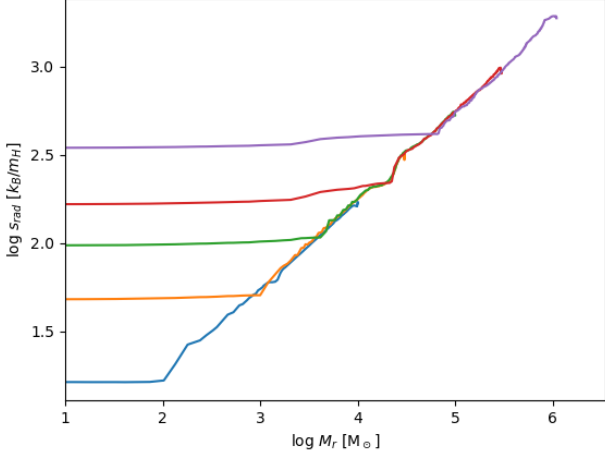


Fig. 7. Same as Figure 6 for the model at $Z = 3 Z_{\odot}$ and $\dot{M} = 100 M_{\odot} \text{ yr}^{-1}$.

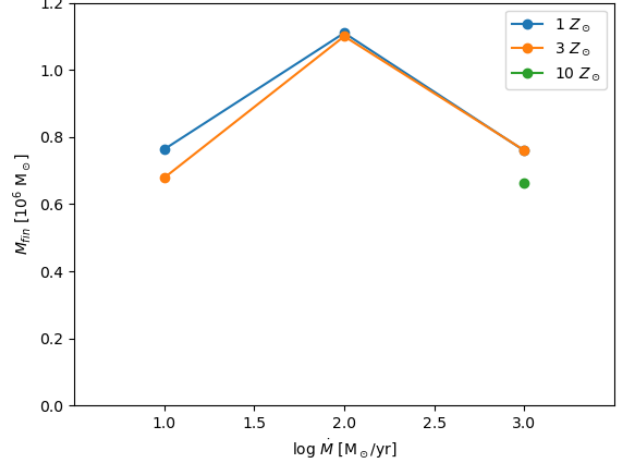


Fig. 9. Final mass at GR instability as a function of the accretion rate, for the indicated metallicities.

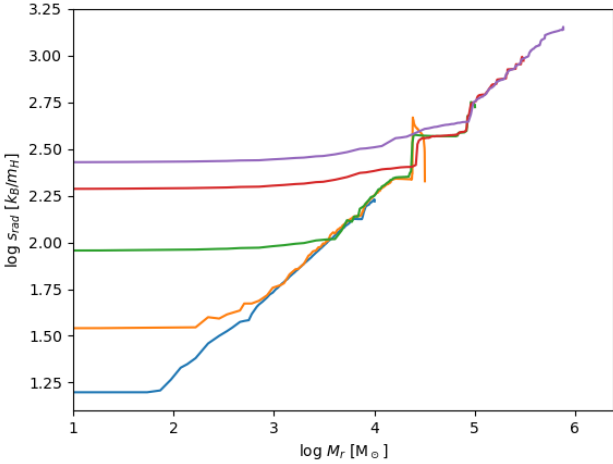


Fig. 8. Same as Figure 6 for the model at $Z = 3 Z_{\odot}$ and $\dot{M} = 1000 M_{\odot} \text{ yr}^{-1}$.

4. Discussion

4.1. Evolutionary tracks on the HR diagram

The evolutionary tracks of all the models remain in the red on the HR diagram, showing no sign of contraction towards the blue until the GR instability, at luminosities $10^{10} - 10^{11} L_{\odot}$. This is in contrast with the zero-metallicity case, where the tracks start to move to the blue at these luminosities (Hosokawa et al. 2013; Haemmerlé et al. 2018b; Nandal et al. 2024). We interpret this difference as the effect of the larger number density of free electrons for higher metallicity, so that the photosphere is locked on the Hayashi limit towards lower gas densities (Haemmerlé et al. 2019). This fact is key for the problem of the ionising feedback, in particular in the case where other effects postpone the GR instability (rotation, dark matter; Haemmerlé 2021b, 2024). Indeed, in case the star moves to the blue for masses $\gtrsim 10^5 M_{\odot}$, the strong ionising feedback could prevent further accretion (Hosokawa et al. 2011, 2016), limiting the mass to

$\sim 10^5 M_{\odot}$. Here, we see that, for metallicities $\geq Z_{\odot}$, the ionising feedback is expected to remain weak up to masses of at least $\sim 10^6 M_{\odot}$.

4.2. Internal structures

As shown already in Haemmerlé et al. (2019) and Haemmerlé (2020) for lower metallicities, when accretion proceeds at rates $\gtrsim 10 M_{\odot} \text{ yr}^{-1}$, the structure of the star is well approximated by hylotropes (Begelman 2010), made of an isentropic core and a radiative envelope where entropy grows outwards like $s \propto M_r^{1/2}$. At these rates, the evolutionary timescale, set by accretion ($t \sim M/\dot{M}$), is shorter than the Kelvin-Helmholtz (KH) timescale, which prevents any loss of entropy by radiative transfer. The Lagrangian layers of the radiative zone are nevertheless contracting (Figures 2-3-4-5). However this is not a KH contraction, but an adiabatic compression driven by accretion: the weight of the accreted gas induces an increase in the pressure in the whole star, and so in the density. As a consequence, the evolution is driven by accretion, all the other processes being too slow to produce any effect. It implies that the structure of the star is essentially given by the stellar mass, independently of the accretion rate. On the other hand, another consequence of the adiabaticity of the evolution is that the successive entropy profiles match each other in the radiative zone: each Lagrangian layer keeps the entropy it advected at accretion. It follows that the oscillations of the surface visible in Figures 1-2-3-4-5 have an impact on the whole stellar structure, in particular on the size of the convective core.

The evolutionary tracks on the $M_{\text{core}} - M$ diagram are shown in Figure 10 for the models at $Z = 3 Z_{\odot}$. Once the star is supermassive and H-burning has started, the convective core represents typically 10% of the total stellar mass. For a given mass, the model at $\dot{M} = 10 M_{\odot} \text{ yr}^{-1}$ has a more massive core than the models with larger accretion rates. This is because of the longer evolutionary timescale in this model, that allows for entropy losses, so that the layers have the time to contract via a KH contraction, and to join the core that becomes more massive for a given total mass. On the other hand, for the models at $100 - 1000 M_{\odot} \text{ yr}^{-1}$, this effect disappears due to the short

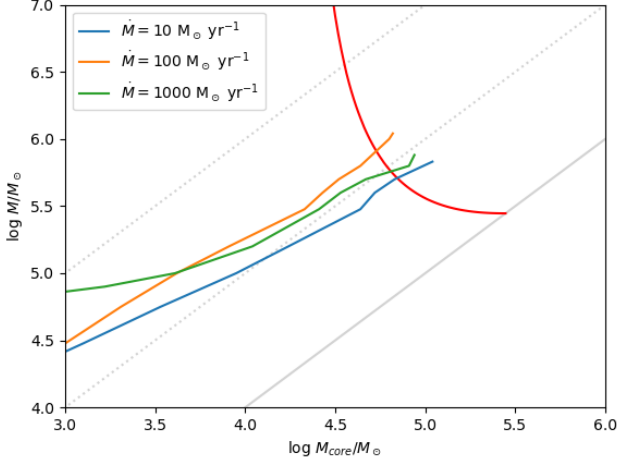


Fig. 10. $M_{\text{core}} - M$ diagram of the models at $Z = 3 Z_{\odot}$, for the indicated accretion rates. The red line is the hylotropic stability limit with $\mu = 0.64$ and $T_c = 7 \times 10^7$ K. The grey diagonals indicate constant fractions $M_{\text{core}}/M = 1\% - 10\% - 100\%$.

evolutionary timescales, so that the $M_{\text{core}} - M$ relation is nearly unique. Actually, we can see that, for a given mass, this is the model with the shorter timescale that has the more massive core. In this regime of extreme accretion, the evolution of the core is impacted by the advection of the intermediate convective zones, that reflect the oscillations at the stellar surface, as described above. In particular, we can see that the oscillations of the surface at $M \sim 30\,000 M_{\odot}$ in the model at $\dot{M} = 1000 M_{\odot} \text{ yr}^{-1}$ (Figure 4) translate into oscillations in the $M_{\text{core}} - M$ relation when the layers accreted during the oscillations join the convective core, that is when $M_{\text{core}} \sim 30\,000 M_{\odot}$. At this point, the convective core is growing rapidly due to the advection of a series of isentropic layers, which explains why this model has a larger core than the model at $\dot{M} = 100 M_{\odot} \text{ yr}^{-1}$ for a given mass.

Finally, we notice that another reason why the 'radiative' zone is prone to transient convective instabilities is that the adiabatic and radiative gradients are both very close to $1/4$ in the Eddington limit:

$$\nabla_{\text{ad}} = \frac{4 - 3\beta}{16 - 12\beta - \frac{3}{2}\beta^2} = \frac{1}{4} + O(\beta^2) \quad (21)$$

$$\begin{aligned} \nabla_{\text{rad}} &= \frac{3\kappa P L_r}{16\pi a c T^4 G M_r} = \frac{1}{4} \frac{1}{1 - \beta} \frac{\kappa L_r}{4\pi c G M_r} = \frac{1}{4} \frac{1}{1 - \beta} \frac{dP_{\text{rad}}}{dP} \quad (22) \\ &= \frac{1}{4} \left(1 + \frac{d \ln(1 - \beta)}{d \ln P} \right) = \frac{1}{4} \left(1 - \beta \frac{d \ln \beta}{d \ln P} \right) + O(\beta^2) \quad (23) \end{aligned}$$

where we have used the equations of radiative transfer and of hydrostatic equilibrium. We notice the absence of a $O(\beta)$ term in the adiabatic gradient.

4.3. Final masses

All the models reach the GR instability during H-burning, so that there is no dark collapse in the sense proposed by Nandal et al. (2024).

All the final masses are $\sim 10^6 M_{\odot}$, with a weak dependence on the accretion rate and on the metallicity. In particular, the increase in the accretion rate from 100 to $1000 M_{\odot} \text{ yr}^{-1}$ does not

translate into an increase of the final mass as for lower rates. This fact has already been noticed by Nagele & Umeda (2024) for lower metallicities, but left without explanation. Here we propose an explanation: because of the adiabaticity of the evolution in this extreme accretion regime, the stellar structure is determined by the mass only, nearly independently of the accretion rate, as explained in the previous section, so that we can expect a unique final mass for rates $\gtrsim 100 M_{\odot} \text{ yr}^{-1}$. Only the differences in the oscillations of the stellar surface, kept in memory by the gas when it joins the convective core, impact the core's mass. It leads to a larger core (for given mass) for the model at $\dot{M} = 1000 M_{\odot} \text{ yr}^{-1}$ compared to the one at $\dot{M} = 100 M_{\odot} \text{ yr}^{-1}$ (Figure 10). As a consequence, the GR instability is reached at a lower mass for the model at $\dot{M} = 1000 M_{\odot} \text{ yr}^{-1}$ than for the one at $\dot{M} = 100 M_{\odot} \text{ yr}^{-1}$.

Figure 10 compares the final mass of the models at $Z = 3 Z_{\odot}$ with the hylotropic stability limit (Haemmerlé 2020). The hylotropic limit is computed for a mean molecular weight $\mu = 0.64$ and a central temperature $T_c = 7 \times 10^7$ K, typical values for $Z = 3 Z_{\odot}$ SMSs in the beginning of H-burning. We see that the models exceed slightly this analytic limit, but by a maximum of 0.2 dex in M . Thus, the hylotropic limit represents a good approximation for the models. It illustrates that the larger is the convective core the smaller is the final mass, explaining why the model at $\dot{M} = 1000 M_{\odot} \text{ yr}^{-1}$ has a smaller final mass than that at $\dot{M} = 100 M_{\odot} \text{ yr}^{-1}$.

5. Conclusion

In the present work, we studied for the first time the properties of SMSs at $Z > Z_{\odot}$, focusing on the conditions met in galaxy merger driven direct collapse ($Z = 1 - 10 Z_{\odot}$, $\dot{M} = 10 - 1000 M_{\odot} \text{ yr}^{-1}$). We neglected rotation, which will be the topic of the next paper of the series.

We found that, at these accretion rates and metallicities, SMSs evolve as red supergiant protostars until the GR instability (Figure 1). The internal structure is made of an isentropic convective core that contains $\sim 10\%$ of the total stellar mass, a 'radiative' region full of small transient convective zones, where entropy grows outwards, following a hylotropic law, and a thin convective envelope with an entropy decreasing outwards due to the non-adiabaticity of convection in the low density regions (Figures 2-3-4-5-6-7-8). For accretion rates $> 10 M_{\odot} \text{ yr}^{-1}$, the evolution in the radiative region is adiabatic (Figures 7-8): the Lagrangian layers are contracting, however this is not a KH contraction, but an adiabatic compression driven by accretion. As a consequence, in this extreme accretion regime, the stellar structure is set essentially by the stellar mass, independently of the accretion rate. This fact results in a nearly unique final mass $\sim 10^6 M_{\odot}$ for all the models (Figure 9). Moreover, all the models reach the GR instability during H-burning.

References

- Asplund, M., Grevesse, N., & Sauval, A. J. 2005, in *Astronomical Society of the Pacific Conference Series*, Vol. 336, *Cosmic Abundances as Records of Stellar Evolution and Nucleosynthesis*, ed. T. G. Barnes, III & F. N. Bash, 25
- Bañados, E., Venemans, B. P., Mazzucchelli, C., et al. 2018, *Nature*, 553, 473
- Begelman, M. C. 2010, *MNRAS*, 402, 673
- Bogdán, Á., Goulding, A. D., Natarajan, P., et al. 2024, *Nature Astronomy*, 8, 126
- Bromm, V., Coppi, P. S., & Larson, R. B. 2002, *ApJ*, 564, 23
- Bromm, V. & Loeb, A. 2003, *ApJ*, 596, 34
- Chandrasekhar, S. 1964, *ApJ*, 140, 417
- Chon, S., Hosokawa, T., & Yoshida, N. 2018, *MNRAS*, 475, 4104

- Dijkstra, M., Haiman, Z., Mesinger, A., & Wyithe, J. S. B. 2008, *MNRAS*, 391, 1961
- Eggenberger, P., Meynet, G., Maeder, A., et al. 2008, *Ap&SS*, 316, 43
- Haemmerlé, L. 2020, *A&A*, 644, A154
- Haemmerlé, L. 2021a, *A&A*, 647, A83
- Haemmerlé, L. 2021b, *A&A*, 650, A204
- Haemmerlé, L. 2024, *A&A*, 689, A202
- Haemmerlé, L., Eggenberger, P., Meynet, G., Maeder, A., & Charbonnel, C. 2016, *A&A*, 585, A65
- Haemmerlé, L., Klessen, R. S., Mayer, L., & Zwick, L. 2021, *A&A*, 652, L7
- Haemmerlé, L., Mayer, L., Klessen, R. S., et al. 2020, *Space Sci. Rev.*, 216, 48
- Haemmerlé, L., Meynet, G., Mayer, L., et al. 2019, *A&A*, 632, L2
- Haemmerlé, L., Woods, T. E., Klessen, R. S., Heger, A., & Whalen, D. J. 2018a, *ApJ*, 853, L3
- Haemmerlé, L., Woods, T. E., Klessen, R. S., Heger, A., & Whalen, D. J. 2018b, *MNRAS*, 474, 2757
- Haiman, Z., Rees, M. J., & Loeb, A. 1997, *ApJ*, 476, 458
- Herrington, N. P., Whalen, D. J., & Woods, T. E. 2023, *MNRAS*, 521, 463
- Hosokawa, T., Hirano, S., Kuiper, R., et al. 2016, *ApJ*, 824, 119
- Hosokawa, T., Omukai, K., & Yorke, H. W. 2012, *ApJ*, 756, 93
- Hosokawa, T., Omukai, K., Yoshida, N., & Yorke, H. W. 2011, *Science*, 334, 1250
- Hosokawa, T., Yorke, H. W., Inayoshi, K., Omukai, K., & Yoshida, N. 2013, *ApJ*, 778, 178
- Klessen, R. S. & Glover, S. C. O. 2023, *ARA&A*, 61, 65
- Kokorev, V., Fujimoto, S., Labbe, I., et al. 2023, *ApJ*, 957, L7
- Kovács, O. E., Bogdán, A., Natarajan, P., et al. 2024, *ApJ*, 965, L21
- Larson, R. L., Finkelstein, S. L., Kocevski, D. D., et al. 2023, *ApJ*, 953, L29
- Latif, M. A., Schleicher, D. R. G., Schmidt, W., & Niemeyer, J. C. 2013, *MNRAS*, 436, 2989
- Maiolino, R., Scholtz, J., Witstok, J., et al. 2024, *Nature*, 627, 59
- Mayer, L., Capelo, P. R., Zwick, L., & Di Matteo, T. 2024, *ApJ*, 961, 76
- Mayer, L., Fiacconi, D., Bonoli, S., et al. 2015, *ApJ*, 810, 51
- Mayer, L., Kazantzidis, S., Escala, A., & Callegari, S. 2010, *Nature*, 466, 1082
- Mortlock, D. J., Warren, S. J., Venemans, B. P., et al. 2011, *Nature*, 474, 616
- Nagele, C. & Umeda, H. 2024, *Phys. Rev. D*, 110, L061301
- Nagele, C., Umeda, H., Takahashi, K., Yoshida, T., & Sumiyoshi, K. 2022, *MNRAS*, 517, 1584
- Nandal, D., Regan, J. A., Woods, T. E., et al. 2023, *A&A*, 677, A155
- Nandal, D., Zwick, L., Whalen, D. J., et al. 2024, *A&A*, 689, A351
- Omukai, K. 2001, *ApJ*, 546, 635
- Regan, J. A., Visbal, E., Wise, J. H., et al. 2017, *Nature Astronomy*, 1, 0075
- Saio, H., Nandal, D., Ekström, S., & Meynet, G. 2024, *A&A*, 689, A169
- Umeda, H., Hosokawa, T., Omukai, K., & Yoshida, N. 2016, *ApJ*, 830, L34
- Wang, F., Yang, J., Fan, X., et al. 2021, *ApJ*, 907, L1
- Wang, F., Yang, J., Fan, X., et al. 2018, *ApJ*, 869, L9
- Woods, T. E., Agarwal, B., Bromm, V., et al. 2019, *PASA*, 36, e027
- Woods, T. E., Heger, A., Whalen, D. J., Haemmerlé, L., & Klessen, R. S. 2017, *ApJ*, 842, L6
- Woods, T. E., Patrick, S., Elford, J. S., Whalen, D. J., & Heger, A. 2021, *ApJ*, 915, 110
- Woods, T. E., Patrick, S., Whalen, D. J., & Heger, A. 2024, *ApJ*, 960, 59
- Wu, X.-B., Wang, F., Fan, X., et al. 2015, *Nature*, 518, 512
- Yang, J., Wang, F., Fan, X., et al. 2020, *ApJ*, 897, L14
- Zwick, L., Mayer, L., Haemmerlé, L., & Klessen, R. S. 2023, *MNRAS*, 518, 2076